

1 **SPHERICAL SHALLOW WATER WAVES SIMULATION BY A CUBED SPHERE**
2 **FINITE DIFFERENCE SOLVER**

3 M. BRACHET†AND J.-P. CROISILLE‡

4 †*Univ. Grenoble Alpes, CNRS, Grenoble INP*, LJK, 38000 Grenoble, France*

5 ‡*Univ. de Lorraine, CNRS, IECL, 57000 Metz, France*

ABSTRACT. We consider the test suite for the Shallow Water (SW) equations on the sphere suggested in Shamir & Paldor (2016*b*) and Shamir et al. (2019). This series of tests consists of zonally propagating wave solutions of the linearized Shallow Water (LSW) equations on the full sphere.

Two series of solutions are considered. The first series, Shamir & Paldor (2016*b*), is referred to as "barotropic". It consists of an extension of the Rossby-Haurwitz test case in Williamson et al. (1992). The second series, Shamir et al. (2019), referred to as (Matsuno) "baroclinic", consists of a generalisation of the solution to LSW in an equatorial channel introduced in Matsuno (1966).

The Hermitian Compact Cubed Sphere (HCCS) model which is used in this paper is a Shallow Water solver on the sphere introduced in Brachet & Croisille (n.d.). The spatial approximation is a center finite difference scheme based on high order differencing along great circles. The time stepping is performed by the explicit RK4 scheme or by an exponential scheme. For both test case series, barotropic and baroclinic, the results show a very good agreement of the numerical solution with the analytic one, even for long time simulations.

6 *Keywords: Spherical Shallow Water waves - Inertia-gravity wave - Rossby wave - Cubed Sphere grid -*
7 *Finite difference scheme - Exponential time scheme*

8 1. INTRODUCTION

9 In this paper we consider the Shallow Water equations (SW) on a rotating sphere. These equations serve
10 as a reference system to be solved to assess the accuracy of dynamical cores for meteorology in spherical
11 geometry, Ghil & Childress (1987). The linearized version of SW at an atmosphere at rest is called the
12 LSW system. It represents the minimal wave model of interest on the rotating sphere. It is of foremost
13 importance in climatology and oceanography. As mentioned in the monograph Paldor (2015), LSW is still a
14 topic with many open problems. One of these problems is the derivation of quasi-analytic solutions to LSW.
15 Such solutions are natural candidates to serve as global test cases for SW. Along this line, two new series of
16 test cases for SW have been recently suggested in Shamir & Paldor (2016*b*) and Shamir et al. (2019).

E-mail address: matthieu.brachet@inria.fr*,* jean-pierre.croisille@univ-lorraine.fr*.*

Date: February 29, 2020.

17 The goal of this paper is to assess a particular finite difference method on the sphere using these two series
18 of test cases. The finite difference scheme under consideration uses the equiangular Cubed Sphere, Ronchi
19 et al. (1996). This scheme, called HCCS ¹, can be seen as an extension to the Cubed Sphere of the 4th order
20 compact scheme, widely used in Computational Aeroacoustics (CAA), Yee & Sjögren (2004). The HCCS
21 scheme for the SW equation has been considered in Brachet & Croisille (n.d.), Brachet (2018) and in Croisille
22 (2013, 2015) for the linear convection equation. Very good accuracy and stability properties were observed for
23 a broad series of test cases, Williamson (2007), Galewsky et al. (2004) and R. D. Nair (2008). In analogy to
24 the spectral method, although the design of the spatial approximation is not ab initio conservative, excellent
25 conservation properties are numerically observed.

26 The purpose of the test cases for SW suggested in Shamir & Paldor (2016*b*) and Shamir et al. (2019) is
27 to assess the accuracy of dynamical cores for long time simulations. The physical and mathematical analysis
28 of the test cases can be found in De-Leon & Paldor (2011), Paldor et al. (2013) and in Shamir & Paldor
29 (2014, 2016*a*). The family of solutions that are derived are doubly quantified with a couple of integers (k, n) .
30 These integers stand for, respectively, the longitudinal wave number, which determines the wave periods
31 in the zonal direction, and the latitudinal mode number, which determines the number of zero crossings
32 in the meridional direction. Along the meridional direction, depending on the case, either the Gegenbauer
33 or the Hermite polynomial functions are involved ². Both test cases can be considered as new versions of
34 the well known Rossby-Haurwitz test in Williamson et al. (1992). The first test case is concerned with
35 the barotropic context, (thick atmosphere layer, "fast" inertia-gravity waves). The second test is concerned
36 with the baroclinic context, (thin atmosphere layer, "slow" inertia-gravity waves). For these two tests, the
37 emphasis is on the fact that a dynamical core must be able to maintain stability and accuracy, even after a
38 very large number of time iterations.

39 In the present paper, we show that the recently introduced HCCS solver Brachet & Croisille (n.d.) is able
40 to accurately calculate each of these tests. In all cases, the simulated final time corresponds to many wave
41 periods, in particular for the Rossby type solutions.

42 The outline of the paper is as follows. In Section 2 we recall the principle of the spherical approximation
43 with the HCCS scheme. In Section 3, we summarize the derivation of the quasi-analytical solutions for LSW,
44 as presented in Shamir & Paldor (2014, 2016*a*). The set up of both test cases with the HCCS formalism is
45 given in Section 4. The numerical results for the barotropic and the baroclinic cases are reported in Section 5
46 and Section 6 respectively. Conservation properties are reported in detail in Section 7. Concluding remarks
47 and perspectives are given in Section 8.

¹HCCS stands for Hermitian Compact Cubed Sphere

²In contrast, for Spherical Harmonics, the associated Legendre polynomials are involved

In this section, the Hermitian Compact Scheme on the Cubed Sphere (HCCS) is summarized Croisille (2013, 2015), Brachet (2018) and Brachet & Croisille (n.d.). Consider the spherical Shallow Water equations (SW):

$$(1) \quad (\text{SW}) \quad \begin{cases} \frac{\partial h^*}{\partial t}(t, \mathbf{x}) + \nabla_T \cdot (h^*(t, \mathbf{x}) \mathbf{u}(t, \mathbf{x})) = 0, \\ \frac{\partial \mathbf{u}}{\partial t}(t, \mathbf{x}) + \nabla_T \left(\frac{1}{2} |\mathbf{u}(t, \mathbf{x})|^2 + gh(t, \mathbf{x}) \right) + (f(\mathbf{x}) + \zeta(t, \mathbf{x})) \mathbf{n}(\mathbf{x}) \times \mathbf{u}(t, \mathbf{x}) = \mathbf{0}. \end{cases}$$

In (1), the unknown is $(t, \mathbf{x}) \in \mathbb{R}_+ \times \mathbb{S}_a \mapsto \mathbf{q}(t, \mathbf{x}) = [h(t, \mathbf{x}), \mathbf{u}(t, \mathbf{x})]^T$, with h the height of the atmosphere and \mathbf{u} the tangential wind velocity. The *relative vorticity* is $\zeta = (\nabla_T \times \mathbf{u}) \cdot \mathbf{n}$ and $h^*(t, \mathbf{x}) = h(t, \mathbf{x}) - h_s(\mathbf{x})$ with h_s the bottom topography function. The subscript T denotes tangential operators. The Coriolis force is $f(\mathbf{x}) = 2\Omega \sin(\theta)$, where θ is the latitude angle and Ω the angular earth velocity. Equation (1) is rewritten as

$$(2) \quad \partial_t \mathbf{q}(t, \mathbf{x}) = F(\mathbf{q}(t, \mathbf{x})),$$

where $\mathbf{q}(\mathbf{x}) \mapsto F(\mathbf{q})(\mathbf{x})$ denotes

$$(3) \quad F(\mathbf{q})(\mathbf{x}) = - \begin{bmatrix} \nabla_T \cdot (h^* \mathbf{u}) \\ \nabla_T \left(\frac{1}{2} |\mathbf{u}|^2 + gh \right) + (f + \zeta) \mathbf{n} \times \mathbf{u} \end{bmatrix}.$$

Consider a function $\mathbf{q}(t, \mathbf{x}) = \bar{\mathbf{q}} + \mathbf{q}'(t, \mathbf{x})$, with $\bar{\mathbf{q}} = [\bar{h} = H, \bar{\mathbf{u}} = \mathbf{0}]^T$ an atmosphere at rest with fixed height H . The perturbation is $\mathbf{q}'(t, \mathbf{x})$:

$$(4) \quad \mathbf{q}'(t, \mathbf{x}) = [h'(t, \mathbf{x}), \mathbf{u}'(t, \mathbf{x})]^T, \quad \mathbf{u}' = [u', v'].$$

With the notation

$$(5) \quad \bar{J} = J_{\alpha, \beta} = \partial_\beta F_\alpha(\bar{\mathbf{q}}), \quad \alpha, \beta = 1, \dots, 3,$$

the linearization of (2) at $\bar{\mathbf{q}}$ is

$$(6) \quad \partial_t q'_\alpha(t, \mathbf{x}) = \bar{J}_{\alpha\beta} q'_\beta(t, \mathbf{x}), \quad (\text{summation over } \beta),$$

or equivalently

$$(7) \quad (\text{LSW}) \quad \begin{cases} \frac{\partial h'(t, \mathbf{x})}{\partial t} + H \nabla_T \cdot \mathbf{u}'(t, \mathbf{x}) = 0, \\ \frac{\partial \mathbf{u}'(t, \mathbf{x})}{\partial t} + g \nabla_T h'(t, \mathbf{x}) + f(\mathbf{x}) \mathbf{n}(\mathbf{x}) \times \mathbf{u}'(t, \mathbf{x}) = \mathbf{0}. \end{cases}$$

64 The HCCS scheme provides an approximation in space of (1). It is based on the equiangular Cubed Sphere,
65 which is a particular grid of the sphere. This grid is decomposed in six panels matching the six faces of a cube
66 Ronchi et al. (1996). In recent years, Cubed Sphere grids have become a standard in numerical climatology.
67 Different kinds of Cubed Spheres do exist, Purser & Rancic (1998). Cubed Spheres are commonly used as
68 a tiling of the sphere for conservative approximations. In this case, the cells defined by the Cubed Sphere
69 serve for discrete averaging. Examples of conservative approximations on the Cubed Sphere include the finite
70 volume method, the discontinuous Galerkin method and the spectral element method. In the contrary, in
71 our case, the nodes of the Cubed Sphere serve as unknown location for finite differencing. The nodes are
72 denoted by

$$(8) \quad \begin{cases} \mathbf{s}_{i,j}^k, & k = (I), (II), \dots (VI) = \text{panel index,} \\ -N/2 \leq i, j \leq N/2 = \text{horizontal and vertical index.} \end{cases}$$

73 Let $\mathbf{q}(\mathbf{x})$ be a function defined for $\mathbf{x} \in \mathbb{S}_a$, ($a = \text{earth radius}$). A gridfunction approximating \mathbf{q} is denoted by
74 $\mathbf{q} = [\mathbf{q}_{i,j}^k]^T$ with

$$(9) \quad \mathbf{q}(\mathbf{s}_{i,j}^k) \simeq \mathbf{q}_{i,j}^k, \quad k = (I), (II), \dots (VI), \quad -N/2 \leq i, j \leq N/2.$$

75 In the HCCS scheme, advantage is taken of coordinate lines of the equiangular Cubed Sphere. These coor-
76 dinate lines are sections of great circles along which finite differencing is operated. The finite differencing is
77 the standard fourth order (compact) scheme which reads

$$(10) \quad \frac{1}{6}u_{\xi,j-1} + \frac{2}{3}u_{\xi,j} + \frac{1}{6}u_{\xi,j+1} = \frac{u_{j+1} - u_{j-1}}{2\Delta\xi},$$

78 where $\xi \in [0, 2\pi)$ stands for an angle along a great circle and $\Delta\xi = 2\pi/N$ is the angular step size. This permits
79 to define centered approximations to the gradient, the divergence and the curl, denoted with subscript Δ :

$$(11) \quad \nabla_T h(\mathbf{s}_{i,j}^k) \simeq \nabla_{T,\Delta} h(\mathbf{s}_{i,j}^k), \quad \nabla_T \cdot \mathbf{u}(\mathbf{s}_{i,j}^k) \simeq \nabla_{T,\Delta} \cdot \mathbf{u}(\mathbf{s}_{i,j}^k), \quad \nabla_T \times \mathbf{u}(\mathbf{s}_{i,j}^k) \simeq \nabla_{T,\Delta} \times \mathbf{u}(\mathbf{s}_{i,j}^k).$$

80 The analytical solution $\mathbf{q}(t, \mathbf{x}) = [h(t, \mathbf{x}), \mathbf{u}(t, \mathbf{x})]^T$ is approximated by the numerical solution

$$(12) \quad \mathbf{q}(t) = [\mathbf{h}_{i,j}^k(t), \mathbf{u}_{i,j}^k(t)]^T, \quad k = (I), (II), \dots (VI), \quad -N/2 \leq i, j \leq N/2.$$

81 The discrete system for $\mathbf{q}(t)$ is deduced from (1) by

- 82 • replacing $\mathbf{q}(t, \mathbf{x})$ by $\mathbf{q}(t)$.
- 83 • replacing all differential operators ∇_T by their discrete approximations $\nabla_{T,\Delta}$ defined in (11).

84

85 This provides the semi-discrete HCCS solver, which reads

$$(13) \quad \partial_t \mathbf{q}(t) = F_\Delta(\mathbf{q}(t)),$$

86 where $F_\Delta(\mathbf{q})$ is defined by

$$(14) \quad F_\Delta(\mathbf{q}) = F_\Delta([\mathbf{h}_{i,j}^k, \mathbf{u}_{i,j}^k]^T) = - \begin{bmatrix} \nabla_{T,\Delta} \cdot [\mathbf{h}_{i,j}^{*k} \mathbf{u}_{i,j}^k]^T \\ \nabla_{T,\Delta} \left[\frac{1}{2} |\mathbf{u}_{i,j}^k|^2 + g \mathbf{h}_{i,j}^k \right]^T + [(f_{i,j}^k + \zeta_{i,j}^k) \mathbf{n}_{i,j}^k \times \mathbf{u}_{i,j}^k]^T \end{bmatrix}.$$

87 In (14), $\zeta_{i,j}^k = (\nabla_{T,\Delta} \times \mathbf{v}_{i,j}^k) \cdot \mathbf{n}_{i,j}^k$ is the semi-discrete relative vorticity. The main properties of the HCCS
88 solver, reported in Brachet & Croisille (n.d.), are the following:

- 89 • It is fully centered for the vector $\mathbf{q}_{i,j}^k$.
- 90 • It is fourth order accurate with respect to $\Delta = \Delta\xi = \Delta\eta$, where (ξ, η) stands for the local coordinate
91 system on a panel.

92 Several time stepping schemes have been proved to be efficient to integrate (14) in time. Specifically in this
93 paper, we display results obtained with two time schemes. First the explicit RK4 scheme is used, subject to a
94 stability condition $\text{CFL} \leq 1$. The second time stepping is a particular exponential scheme of the Rosenbrock
95 family, (Hairer & Wanner 1991, chap.7), referred as ERK2 in the sequel. Several studies have found this
96 scheme as a relevant option for spherical SW problems. Refer to Clancy & Pudykiewicz (2013) and Brachet &
97 Croisille (n.d.). The efficiency of the ERK2 scheme for the test series presented is confirmed here. In all cases
98 a spatial filtering is added at each time step. This filter consists in an hyperdiffusion term operated along
99 the great circles of the Cubed Sphere. This hyperdiffusion step has been found a suitable way to enhance
100 stability without destroying high accuracy. Details on recent results with the HCCS solver and various time
101 steppings are reported in Brachet & Croisille (n.d.).

102 3. LSW SOLUTIONS AS APPROXIMATIONS OF SW EQUATIONS

103 **3.1. Zonally propagating waves.** Assessing accuracy and stability of dynamical cores with suitable test
104 cases has become an essential task in numerical meteorology. A well known test series for SW over the
105 sphere is Williamson et al. (1992). This test series is a standard that any SW solver must successfully pass.
106 Number 6 in Williamson et al. (1992) is the well known Rossby-Haurwitz (RH) test case. This test consists
107 in comparing the SW solution to an analytically known solution of the non divergent barotropic equation
108 (BV). The goal is to observe how the numerical code at hand behaves when simulating the hydrodynamics
109 mode. However, since the BV equation is not the SW equation, when using the initial data of test 6 of
110 Williamson et al. (1992) in a SW solver, acoustic waves are superimposed to the hydrodynamics mode. Thus
111 one does not expect a numerical behaviour conforming to the exact solution of the BV equation: in fact,
112 numerical evidence has shown Thuburn & Li (2000), Paldor (2015) and Ullrich (2011) that the RH initial
113 data evolves in an instability when plugged in a SW numerical solver. As observed in Ullrich (2011), the time
114 of apparition of the instability depends on the particular approximation in space. This instable behaviour
115 was also observed with the HCCS solver Brachet & Croisille (n.d.).

116 This makes the RH test case not suitable to evaluate a SW solver over long times. Overcoming this flaw
 117 was the main purpose for introducing a new series of test cases. In Shamir & Paldor (2016b), Shamir et al.
 118 (2019), the idea is to consider a zonally propagating simple wave solution of (6) of the form:

$$(15) \quad \mathbf{q}'(t, \mathbf{x}) = \tilde{\mathbf{q}}(\theta) \exp(ik(\lambda - Ct)).$$

119 In (15), (λ, θ) is the lon-lat coordinate and k is the wave number in the zonal direction, C is a velocity
 120 parameter and $\tilde{\mathbf{q}}(\theta) = [\tilde{h}(\theta), \tilde{u}(\theta), \tilde{v}(\theta)]^T$ is the amplitude depending on the latitude only. Substituting (15)
 121 in (6) leads to the following spectral problem for the LSW equation, which reads:

$$(16) \quad J(\tilde{\mathbf{q}}(\theta)) = -ikC\tilde{\mathbf{q}}(\theta).$$

122 The spectral problem (16) contains the amplitude $\theta \mapsto \tilde{\mathbf{q}}(\theta)$ and the constant C as unknowns. This is solved
 123 by a dispersion analysis. Let the zonal wavenumber k be fixed. The corresponding possible values of the
 124 couple eigenvalue/eigenvector are found. In the geophysical context, such a spectral analysis is commonly
 125 performed assuming specific a priori hypothesis. Typically, one may assume propagation in an equatorial
 126 or midlatitude channel, and the β - plan for the Coriolis force. Here there is no such assumption. The
 127 eigenfunction $\tilde{\mathbf{q}}(\mathbf{x})$ in (16) is defined *on the full sphere*: the latitude angle $\theta \in (-\pi/2, \pi/2)$ extends up to the
 128 poles and is not limited to a channel.

129 **3.2. Meridional Schrödinger equation.** In a series of works De-Leon & Paldor (2011), Paldor et al.
 130 (2013), Paldor *et al.* suggested to solve the eigenproblem (16) as follows. The problem is approximated by
 131 a differential equation along the meridional direction $\theta \in (-\pi/2, \pi/2)$. This equation is of Schrödinger type.
 132 It is expressed as

$$(17) \quad \frac{d^2}{d\theta^2} \psi(\theta) + F(k, C, \theta) \psi(\theta) = 0, \quad \theta \in (-\pi/2, \pi/2), \quad \psi(\pm\pi/2) = 0.$$

133 In (17), the unknown is the function $\psi(\theta)$. The three components of the vector amplitude $\tilde{\mathbf{q}}(\theta) = [\tilde{h}(\theta), \tilde{u}(\theta), \tilde{v}(\theta)]^T$
 134 are expressed explicitly in terms of $\psi(\theta)$. The equation (17) leads to a quantification with two integers k and
 135 n corresponding to the zonal and latitudinal behaviour. As already mentioned, k stands for a longitudinal
 136 wave number and n for a number of zero crossings in the meridional direction. These two parameters are
 137 here independent. This is in contrast to the standard representation of the Spherical Harmonics, where k
 138 and n are related by $|k| \leq n$. For each couple (k, n) , the characteristic equation of (17) leads to three distinct
 139 phase speeds. These speeds are identified as

- 140 • two inertia-gravity waves (propagating eastward and westward)
- 141 • a Rossby wave

142 This is of course no surprise, since in most wave analysis, whatever the particular a priori hypothesis are,
 143 these three kinds of waves emerge.

144 A second step in the spectral analysis of (17) in Shamir & Paldor (2014, 2016a) is to give a suitable
145 approximation of the wave speeds and of the eigenfunctions. The idea is to expand the amplitude $\tilde{q}(\theta)$ in a
146 discrete basis of orthogonal polynomials. This leads to an approximation which is considered as quasi-exact.
147 How to select a relevant set of polynomials is based on the physical wave regime. Two cases of interest are
148 emphasized, the "thick ocean" and the "thin ocean" regimes, respectively.

149 (1) **Thick ocean regime, Shamir & Paldor (2016a)**: This regime corresponds in (7) to a depth with
150 magnitude $H \simeq 1000\text{m}$. It is referred to as *barotropic*. It corresponds to "fast" acoustic (inertia-
151 gravity) waves with velocity of magnitude 100m s^{-1} .

152 (2) **Thin ocean regime, Shamir & Paldor (2014)**: This regime corresponds in (7) to a depth with
153 magnitude $H \simeq 10\text{m}$. It is referred to as *baroclinic*. This corresponds to slow acoustic waves with
154 velocity of magnitude 10m s^{-1} . This is a more "hydrodynamic" regime. This corresponds to an
155 amplitude function localized near the equator, vanishing close to the poles.

156 In general, the validity of the approximations provided by (15)-(17) depend on the values of k , n and
157 H . Let us only mention here that for moderate values of k and n , the thick ocean regime becomes valid
158 for large values of H of the order of 1000 m or more. A detailed discussion on the choice of polynomial
159 approximations using either the Gegenbauer polynomials or the Hermite polynomials, is presented in Shamir
160 & Paldor (2016b) and Shamir et al. (2019).

161 **3.3. Design of the numerical test cases.** Distinguishing these two physical regimes led to the design of
162 two series of test cases introduced in Shamir & Paldor (2016b) and Shamir et al. (2019) respectively. These
163 tests aim to give a standardization of two particular solutions of the form (15). The main idea on which these
164 two test suites are based is that spherical waves must be approximated with high fidelity by dynamical core
165 models. This underlines the importance of the "pure wave regime" for numerical meteorology and climatology,
166 Müller & O'Brien (1995). The emphasis for these test cases is on accurately evaluating the dispersion and
167 dissipation properties of the numerical method to be assessed, in particular over a long physical time. The
168 notation for the tests and for the error analysis is given in Section 4. There are four tests in all. In Section
169 5, the results with the HCCS solver are displayed for the first test case (barotropic waves). The tests for
170 the thick ocean regime are called Test 1-a (EIG wave) and Test 1-b (Rossby wave). In Section 6, the results
171 for the baroclinic waves are presented, with Test 2-a (EIG wave) and Test 2-b (Rossby wave). To assess the
172 accuracy and stability of the spatial approximation, both cases are considered with different time stepping
173 schemes. Our numerical results were obtained with the explicit RK4 scheme and with a particular exponential
174 scheme (the ERK2 Rosenbrock scheme) ³.

³This kind of numerical assessment is also used in gas dynamics (Euler or Navier-Stokes equations). The accuracy of the nonlinear scheme is assessed when used for wave propagation problems, e.g. occurring in aeroacoustics or turbulence.

176 **4.1. Setting up the test cases.** The implementation of the two series of test cases presented in Section
 177 3.3 proceeds as follows. Test 1 and Test 2 series correspond to the barotropic and the baroclinic waves
 178 respectively. Each series contains an eastward propagating inertia gravity wave referred to as "Test 1-a EIG"
 179 (barotropic) and "Test 2-a EIG" (baroclinic) waves respectively. The Rossby wave in each series is referred to
 180 as "Test 1-b Rossby" (barotropic) and "Test 2-b Rossby" (baroclinic) respectively. In all cases, the analytic
 181 solutions is of the form (15) where parameters specifying the function $q'(t, \mathbf{x})$ in (15) are

- 182 (1) The depth H of the atmosphere at rest.
- 183 (2) The zonal wave number k and mode number n .
- 184 (3) The wave number k is the wavenumber along the zonal direction λ , (longitude direction). The
 185 mode number n corresponds to the meridional direction θ (latitude direction). The analytic solution
 186 involves for the meridional modulation a Gegenbauer polynomial in the barotropic case and a Hermite
 187 polynomial in the baroclinic case. The dispersion analysis with the eigenmodes and the (vector)
 188 eigenfunctions is given in Shamir & Paldor (2014, 2016a) and is not reproduced here. In the Test 1
 189 and and Test 2 series, we have used the routines provided as supplementary material in Shamir &
 190 Paldor (2016b) and Shamir et al. (2019) respectively ⁴. The routines calculate the analytic solutions
 191 in the four cases (1a, 1b, 2a and 2b). In all cases, the constants in front of the amplitude must be
 192 chosen small enough to ensure that the wave (15) be effectively a (quasi) analytic solution.
- 193 (4) In all cases, the numerical solver is the HCCS scheme (13). The initial data at $t = 0$ is the analytic
 194 value given by the matlab routine. It is evaluated at $t = 0$ at the nodes $\mathbf{s}_{i,j}^k$ of the Cubed Sphere. As
 195 already mentionned, the time stepping is performed using various time schemes for comparison. The
 196 explicit fourth order RK4 is our reference scheme. The second order Rosenbrock scheme ERK2 was
 197 used as well. Refer to Clancy & Pudykiewicz (2013) and Brachet & Croisille (n.d.) for comments on
 198 using these time schemes in the context of the SW equations (1).

199 **4.1.1. Test Case 1: barotropic waves.** The input parameters are selected as follows:

- 200 • The atmosphere mean depth is:

$$(18) \quad H = 5000\text{m}.$$

- 201 • The wave numbers k (zonal wave number) and n (meridional wave number) are:

$$(19) \quad (k, n) = (5, 10).$$

- 202 • The wave solutions are as follows:

⁴This supplementary material is also provided in matlab, python and FORTRAN for the Test 1 series and in python for the Test 2 series.

203 (1) Test 1-a is a barotropic inertia gravity wave. It is an Eastward Inertia Gravity wave called EIG
 204 with period 3.16h. Thus 100 periods represent 13.5 days.

205
 206 (2) Test 1-b is a barotropic Rossby wave. It has a period of 12.03 days, (100 periods = 1203 days).

207 The reference Courant number for the EIG wave at the equator is

$$(20) \quad \text{CFL} = \frac{\sqrt{gH}\Delta t}{a\Delta\xi},$$

208 where $a = 6371.22\text{km}$ is the earth radius and $\Delta\xi = a\pi/2N$. The integer N represents the Cubed Sphere
 209 resolution. For example, the reference Courant number $\text{CFL} = 1$ corresponds with $N = 64$ to a time step of
 210 $\Delta t = 699\text{s}$.

211 4.1.2. *Test Case 2: baroclinic waves (Matsuno)*. The input parameters are selected as follows:

- 212 • Atmosphere mean depth:

$$(21) \quad H = 30\text{m}.$$

- 213 • The wave numbers k (zonal wave number) and n (meridional wave number) are

$$(22) \quad (k, n) = (5, 1).$$

214 The two waves are

215 (1) Test 2-a is an EIG (Eastward Inertia Gravity) wave. The period is 1.9 days. Thus 100 periods
 216 represent 190 days.

217
 218 (2) Test 2-b is a Rossby wave with a period of 18.5 days, (100 periods = 1850 days).

219 Compared to (20), the Coriolis force is larger. In this case, the reference Courant number is

$$(23) \quad \text{CFL} = \frac{\Delta t}{a\Delta\xi} \sqrt{gh_0 + \frac{4\Omega^2 a^2 \Delta\xi^2}{6}}.$$

220 The Courant number $\text{CFL} = 1$ corresponds (with a Cubed Sphere resolution $6 \times 64 \times 64$) to a time step
 221 $\Delta t = 8013\text{s}$. This is 10 times larger than for Test 2-a.

222 4.2. **Error notation.** In Sections 5 and 6, the shape of the numerical solutions are shown at initial and
 223 final times. In addition, various errors between the analytical and the calculated solutions are reported. The
 224 analytical solution of (1) is

$$(24) \quad \mathbf{q}(t, \mathbf{x}) = [h(t, \mathbf{x}), \mathbf{u}(t, \mathbf{x})]^T,$$

225 where the velocity \mathbf{u} is decomposed in zonal and meridional components as

$$(25) \quad \mathbf{u} = u_\lambda \mathbf{e}_\lambda + u_\theta \mathbf{e}_\theta.$$

226 The numerical solution (12) is

$$(26) \quad \mathbf{q}(t) = [\mathbf{h}_{i,j}^k(t), \mathbf{u}_{i,j}^k(t)]^T, \quad k = (I), (II), \dots (VI), \quad -N/2 \leq i, j \leq N/2.,$$

227 where the numerical velocity \mathbf{u} is decomposed as

$$(27) \quad \mathbf{u} = \mathbf{u}_\lambda \mathbf{e}_\lambda + \mathbf{u}_\theta \mathbf{e}_\theta.$$

228 (1) *Relative errors*: The relative error on each component is

$$(28) \quad \text{err}_\theta = \frac{\|\mathbf{u}_\theta - u_\theta\|_2}{\|\mathbf{u}_\theta\|_2} \quad \text{and} \quad \text{err}_\lambda = \frac{\|\mathbf{u}_\lambda - u_\lambda\|_2}{\|\mathbf{u}_\lambda\|_2},$$

229 where $\|\cdot\|_2$ denotes the l^2 norm. Similarly for relative error on the height h is given by

$$(29) \quad \text{err}_h = \frac{\|h - \mathbf{h}\|_2}{\|h - H\|_2},$$

230 with \mathbf{h} the numerical total height.

231 (2) *Dispersion error*: As in any discrete approximation of a convective equation, there is a dispersion
 232 error in the HCCS scheme. This dispersion is apparent when one shows the maximum of the error in
 233 function of time. In particular, when the scheme is used over 100 periods, the dispersion is visible.
 234 In this case, as mentioned in Paldor (2015), one is more interested in the preservation of the global
 235 shape of the wave that is represented by the grid than by the numerical velocity which necessarily
 236 slightly differs from the exact one. As suggested in Shamir & Paldor (2016b), the dispersive error is
 237 represented as follows:

- 238 • First, the maximum error is plotted.
- 239 • Second, the dispersion is estimated by the numerical velocity C_n with a Fourier analysis per-
 240 formed on 100 periods and compared to the theoretical velocity C . The relative velocity is
 241 defined by

$$(30) \quad |\Delta C| = \frac{|C - C_n|}{|C|} \times 100.$$

- 242 • Third, Hovmöller diagrams, (see Hovmöller (1949)), are given. Such diagrams provide a suitable
 243 way to represent the accuracy of a numerical scheme for a propagation phenomenon. There are
 244 two variants of Hovmöller diagrams: time/longitude and latitude/time. Both are used in the
 245 sequel.

246 (3) *Dissipation error*: The dissipation is simpler to represent than the dispersion. Here we limit ourselves
 247 to plot the history of the extrema of the total height h . Due to the form (15), the analytical solution
 248 obviously does not have any dissipation and the extrema at any time are the extrema at time $t = 0$.
 249 Therefore, plotting the minimum and maximum of the numerical solution h over a long physical
 250 period of time is a simple and reliable way to represent the dissipation of the numerical solver.

251 5. TEST CASES 1: BAROTROPIC WAVES

252 5.1. Test 1-a: barotropic Eastward Inertia-Gravity (EIG) Wave.

253 Here, we show numerical results
 254 obtained with the HCCS solver for Test 1-a in Section 4.1.1. It is an eastward propagating wave, referred as
 255 EIG. In Fig. 1, the left panel displays the total height h at time $t = 13.5$ days. The time stepping scheme is the
 256 second order accurate Rosenbrock Exponential Integrator (ERK2), (Hairer & Wanner 1991, chap.7). Refer
 257 to Clancy & Pudykiewicz (2013), Brachet & Croisille (n.d.) for more details on using ERK schemes for SW
 258 equations. The right panel displays the history of the relative error. This error increases in function of time
 259 and behaves periodically. This reflects the fact that some error, dispersive and/or dissipative, is necessarily
 260 present in any numerical approximation for convection. On this topic, refer to Shamir & Paldor (2016b). Still
 261 regarding dispersion, the Table 1 reports the magnitude of the relative error on the velocity $|\Delta C|$ defined
 262 in (30). In all cases, the magnitude is smaller than 1%. Another representation of the dispersion is given
 263 in the left and middle panels in Fig. 2. In the left panel, a time longitude Hovmöller diagram is shown.
 264 This diagram is a suitable representation of the characteristics lines of the convection phenomenon at hand
 265 (here the EIG wave) emanating from a parallel at a given latitude. The dashed line represents the numerical
 266 slope, with CFL = 1 (RK4 scheme) and CFL = 4 (ERK2 scheme) respectively. A very good alignment of
 267 the exact and numerical slope can be observed. In the middle panel, a latitude-time Hovmöller diagram is
 268 shown. This second kind of Hovmöller diagram allows to illustrate the temporal changes as opposed to an
 269 instantaneous snapshot. Such a representation was used in Shamir et al. (2019). Finally in the right panel,
 270 the dissipation of the HCCS solver is represented using the history of the extrema (maximum and minimum)
 271 of the total height h . As can be observed, the maximum and the minimum values are almost constant during
 272 100 time periods. This shows that the center solver HCCS is almost dissipation free in this case. The results
 273 obtained with a second ERK scheme (the ERK3 scheme), for which we refer to Clancy & Pudykiewicz (2013),
 274 Brachet & Croisille (n.d.), are similar with the RK4 time scheme or with the ERK2 scheme. These results
 275 are not reported here. For a given scheme assumed to be stable, the results are not sensible to the value of
 the Courant number.

276 5.2. Test 1-b: barotropic Rossby Wave.

277 Here we consider the so called barotropic Rossby wave, whose
 278 setup is given in Section 4.1.1. Again the HCCS solver is used to operate the simulation during 100 periods
 (1203 days). In Fig. 3, left panel, the total height at final time is reported. In the right panel, the maximum

279 error history for h, u_λ, u_θ is reported. As expected, (see Shamir & Paldor (2016b)), due to a small dispersion
 280 error, these errors oscillate periodically. The velocity error is $|\Delta C| = 2.2722\%$ with the ERK2 scheme and
 281 a Courant number $CFL = 16$. With the RK4 scheme and a Courant number $CFL = 0.9$, the error is
 282 $|\Delta C| = 1.7661\%$. In both cases, this is slightly larger than the results for the EIG wave reported in Table 1.
 283 However, the level of the error remains quite good.

284 As for the EIG wave, we also report in Fig. 4 a dispersion analysis based on the time/longitude and
 285 latitude/time Hovmöller diagrams in the left and middle panels respectively. In both cases, the numerical
 286 (dashed line) and theoretical slopes are well aligned. The dissipation of the HCCS solver is reported in
 287 the right panel using the history of the extrema of the total height over the full simulation (1200 days, 100
 288 periods). As for the EIG wave, this shows that the HCCS is visually dissipation free at final time when using
 289 the Cubed Sphere with resolution $6 \times 64 \times 64$. Note that the Cubed Sphere resolution $6 \times 32 \times 32$ is not
 290 sufficient in this case and gives a significant dissipation.

291 6. TEST CASE 2: MATSUNO BAROCLINIC WAVES

292 In this section, we display numerical results obtained with the HCCS solver in the case of the baroclinic
 293 waves test cases presented in Section 4.1.2. As in Section 5, numerical results with the HCCS solver are
 294 reported for two waves: an EIG wave (Test 2-a) and a Rossby wave (Test 2-b). The numerical results for the
 295 total height \mathfrak{h} for both the EIG and the Rossby waves are shown in Fig. 5. The final time is 190 days and
 296 1850 days, respectively, and corresponds to 100 periods in both cases. The history of the errors is shown in
 297 Fig. 6. As in the barotropic test series, the increasing error history expectedly reflects the (small) dispersion
 298 of the scheme, see Shamir & Paldor (2016b). As before, Figs. 7, 8 report the two Hovmöller, time/longitude
 299 and latitude/time, to better visualize the dispersion (left and middle panels). The RK4 and the ERK2 time
 300 stepping schemes are compared. The RK4 scheme is used with a Courant number $CFL = 1$ and the ERK2
 301 scheme is used with a Courant number $CFL = 5$. For both time schemes, the dispersion is very good. Note
 302 that some irregularities are apparent in the latitude/time Hovmöller diagrams when using the ERK2 scheme.
 303 This reflects the choice of the CFL number $CFL = 5$, which is larger than $CFL = 1$. The history of extrema
 304 of \mathfrak{h} in the right panels reflects the dissipation. As before, the HCCS solver appears to be dissipation free with
 305 the $6 \times 64 \times 64$ Cubed Sphere. Table 2 reports the relative error on the velocity ΔC . Notice that different
 306 values of $|\Delta C|$ are obtained whenever different time schemes and different Courant numbers are used. In all
 307 cases, the error on $|\Delta C|$ is small, which is the sign of a small numerical dispersion. For the Test 2-a and Test
 308 2-b, the resolution of the Cubed Sphere for the HCCS solver is $6 \times 64 \times 64$. This is the maximum allowed on
 309 our computer. This is a coarser grid than the one used in Shamir et al. (2019).

311 **7.1. Invariants.** In what follows, the conservation properties obtained in the Test 1 series (Section 5) and in
 312 the Test 2 series (Section 6) are numerically analyzed. The constants are $a = 6.37122 \times 10^6 \text{m}$ (earth radius),
 313 $\Omega = 7.292 \times 10^{-5} \text{s}^{-1}$ (earth angular velocity), and $g = 9.80616 \text{m s}^{-2}$ (gravity constant). The Coriolis force
 314 is $f(\mathbf{x}) = 2\Omega \sin \theta$. The following averaged values are preserved by SW at the continuous level.

$$(31) \quad \left\{ \begin{array}{l} \text{mass: } I_1 = \int_{\mathbb{S}_a^2} h^* ds, \\ \text{energy: } I_2 = \int_{\mathbb{S}_a^2} \frac{1}{2} h^* \mathbf{v}^2 + \frac{1}{2} g (h^2 - h_s^2) ds, \\ \text{potential enstrophy: } I_3 = \int_{\mathbb{S}_a^2} \frac{(\zeta + f)^2}{2h^*} ds \text{ with } \zeta \text{ the relative vorticity,} \\ \text{divergence: } I_4 = \frac{1}{|\mathbb{S}_a|} \int_{\mathbb{S}_a^2} \nabla_T \cdot \mathbf{v} ds, \\ \text{relative vorticity: } I_5 = \frac{1}{|\mathbb{S}_a|} \int_{\mathbb{S}_a^2} (\nabla_T \times \mathbf{v}) \cdot \mathbf{n} ds. \end{array} \right.$$

315 The numerical error for I_1 , I_2 and I_3 is reported using the relative (algebraic) value

$$(32) \quad \frac{I_p(t) - I_p(0)}{I_p(0)}, p = 1, 2, 3.$$

316 The value I_4 and I_5 are reported without scaling.

317 **7.2. Spherical quadrature.** The integral $\int_{\mathbb{S}_a^2} f(\mathbf{x}) d\sigma(\mathbf{x})$ is approximated by $Q_N(f)$, a particular quadrature
 318 rule on the Cubed Sphere. We have used the rule (20) in Portelenelle & Croisille (2018), which is

$$(33) \quad Q_N(f) = a^2 \sum_{k=(I)}^{(VI)} \sum_{i,j=-N/2}^{N/2} \alpha_{i,j} F(\mathbf{s}_{i,j}^k).$$

319 We refer to Portelenelle & Croisille (2018) for the definition of the weights $\alpha_{i,j}$. The numerical integrals in
 320 (31) are evaluated by (33).

321 **7.3. Conservation with the HCCS scheme.** Table 3 reports the conservation of the five quantities mass,
 322 energy, enstrophy, divergence and vorticity at final time for the Test 1 and Test 2 series. The relative
 323 conservation error is excellent in the four cases, ranging from computer accuracy (Baroclinic EIG wave) to
 324 5.10^{-8} (barotropic Rossby wave).

326 The design of test cases based on SW wave (quasi-)solutions of the equations of meteorology is not a
 327 new topic, in 2D or 3D. Refer to Jablonowski & Williamson (2006), Ullrich et al. (2013) and Shamir &
 328 Paldor (2016b) and the references therein. The interest of such solutions is multifaceted. Although being

329 academic, these solutions have the advantage to be close to "real" meteorological models. In addition, such
330 solutions offer an excellent platform for various mathematical aspects of the equations under study. On the
331 one hand, the design of the solutions is interesting in itself. Testing numerical solvers often allows to learn
332 more about the numerical method and its limitation, or about the test case itself. In addition, since very few
333 mathematical results are known on the PDE's (even in the 2D tangential setting), the numerical convergence
334 behaviour of the solver towards "exact" solutions is also a way to learn more.

335 The two new test series suggested in Shamir & Paldor (2016*b*) and Shamir et al. (2019) are a new stimulat-
336 ing family of quasi-analytic solutions of the 2D SW equations. In the present study, they were used to assess
337 the HCCS solver capability to accurately capture essential features, even after as much as 100,000 time iter-
338 ations. In particular, there is no interpanel parasitic reflexion. The numerical results confirm the accuracy of
339 the numerical solver HCCS for spherical convective problems, already observed in Brachet & Croisille (n.d.).
340 Furthermore, as mentionned above, the solver behaves remarkably well regarding conservation. Note that
341 the four test cases are performed with a matlab code on a simple laptop. Typical run times range from 30min
342 for Test2-a (baroclinic EIG wave) to 24h for Test1-b (barotropic Rossby wave), with 100 periods simulated
343 in each case. Clearly, future work is required. First, a numerical convergence analysis could be performed
344 with more computer power. Second, a mathematical analysis of the conservation properties would be useful.
345 Finally, extending the HCCS solver to the full 3D SW equations is clearly an important perspective.

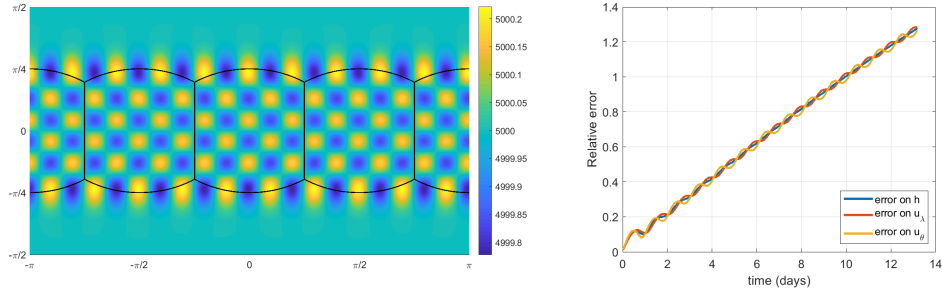


FIGURE 1. Test 1-a (barotropic EIG wave). The final time is $t = 13.5$ days (100 periods). Left panel: total height at final time. Right panel: Histories of relative errors (28-29) for the zonal velocity is u_λ , the meridional velocity u_θ and the total height h . The time scheme is the ERK2 scheme with 407 time iterations and $CFL = 4$, see (20). The resolution of the Cubed-Sphere is $6 \times 64 \times 64$.

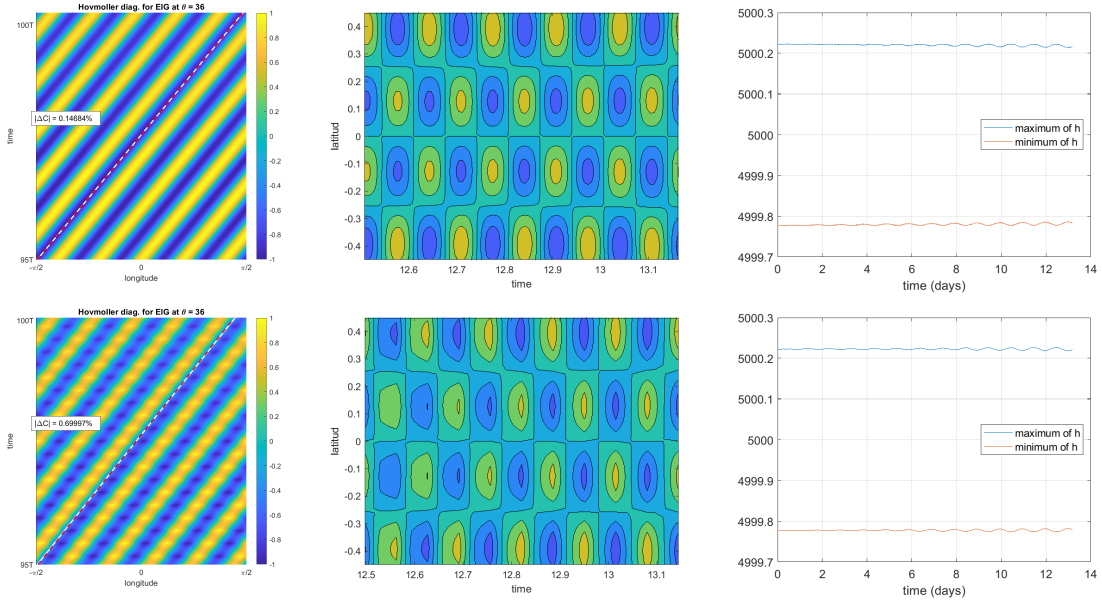


FIGURE 2. Test 1-a (barotropic EIG wave). HCCS solver in space at final time is $t = 13.5$ days (100 periods). First line : RK4 time scheme at $CFL = 0.9$. Second line, ERK2 scheme at $CFL = 4$. The first column corresponds to time-longitude Hovmöller diagrams of the numerical solutions obtained by intersecting the zonal velocity at latitude $\theta = 36$ deg. The dashed line corresponds to the analytic solution. The second column corresponds to latitude-time Hovmöller diagrams obtained by intersecting the zonal velocity at longitude $\lambda = -18$ deg. The third column displays the maximum and the minimum history of the total height h over the full simulation. No significant damping is observed. The Cubed-Sphere resolution is $6 \times 64 \times 64$.

Time scheme	Courant Number CFL	barotrop. EIG wave
ERK2	1	0.6389%
	4	0.6999%
	8	0.4405%
RK4	1	unstable
	0.9	0.1468%

TABLE 1. Test 1-a (barotropic EIG wave). Dispersion analysis at final time $t = 13.5$ days (100 periods). The relative velocity errors $|\Delta C|$ in (30) are reported for various values of CFL. The relative error on the velocity is smaller than 1% in all cases after 100 periods. The RK4 scheme with CFL = 0.9 corresponds to 1808 time iterations and the ERK2 time scheme with CFL = 4 corresponds to 407 time iterations, see (20). Note that the ERK2 is stable with a CFL number as high as CFL = 32. This is not reported in the table since in this case the sample rate is too low to accurately evaluate $|\Delta C|$. The resolution of the Cubed-Sphere is $6 \times 64 \times 64$.

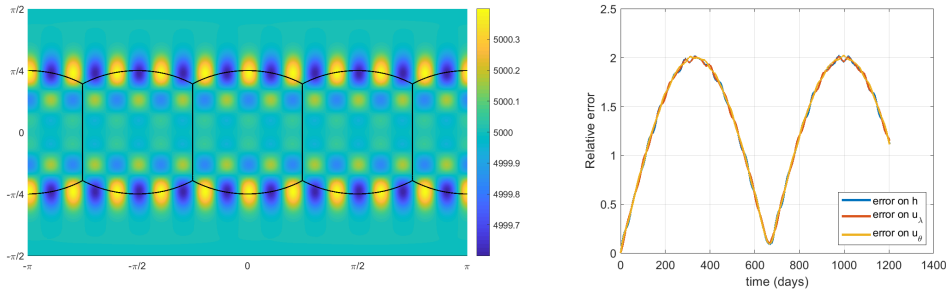


FIGURE 3. Test 1-b (barotropic Rossby wave), HCCS solver in space. The final time is $t = 1203$ days (100 periods). The time scheme is the ERK2 time scheme with 9289 time iterations and CFL = 16, see (20). Left panel: total h at final time. Right panel: history of the relative errors for h , u_λ (zonal velocity) and u_θ (meridional velocity). The three curves are almost superposed. The resolution of the Cubed-Sphere is $6 \times 64 \times 64$.

Time scheme	Courant Number	EIG wave	Rossby wave
RK4	1	0.11156%	0.16333%
ERK2	5	0.44187%	0.18185%
	10	0.44187%	0.28027%

TABLE 2. Test 2-a (baroclinic EIG wave) and Test 2-b (baroclinic Rossby wave). Dispersion analysis. The table reports the relative error $|\Delta C|$ in (30) for the EIG and Rossby waves with the two time schemes RK4 and ERK2. The results are obtained using a Fourier analysis (see Shamir & Paldor (2016b)). For the EIG wave, the final time is $t = 190$ days, (100 periods). The number of time iterations are 2156 (CFL = 1), 431 (CFL = 5) and 215 (CFL = 10). For the Rossby wave, the final time is $t = 1850$ days (100 periods). The number of time iterations are 21565 (CFL = 1), 4313 (CFL = 5) and 2156 (CFL = 10). The Cubed-Sphere grid is $6 \times 64 \times 64$.

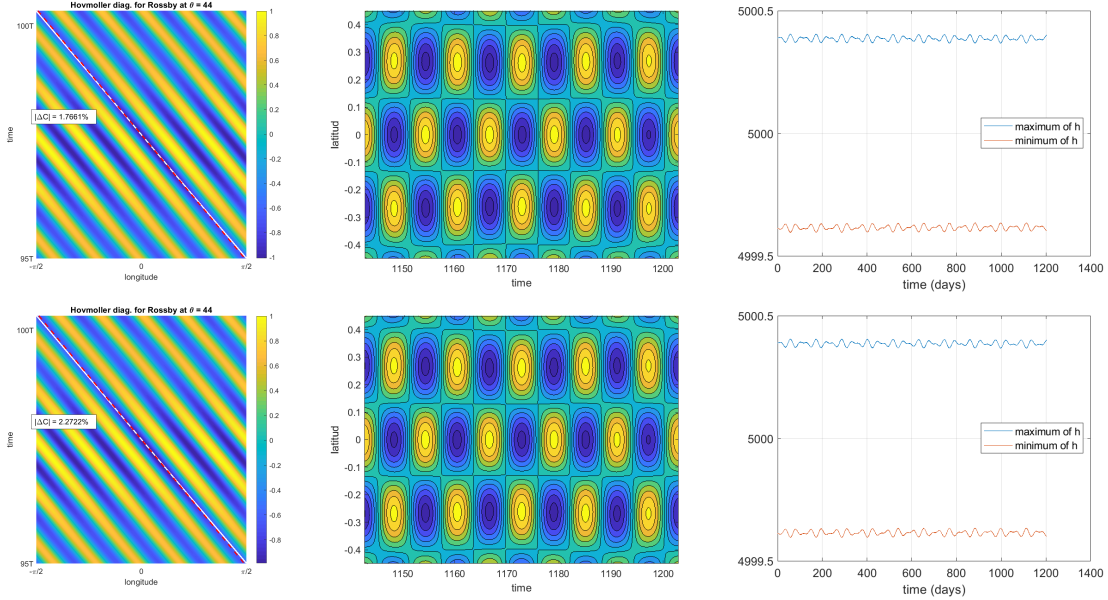


FIGURE 4. Test 1-b (barotropic Rossby wave). Dispersion and dissipation analysis of the HCCS solver at final time (1203 days, 100 periods). First line : RK4 time scheme at CFL = 0.9 and 165143 time iterations. Second line, ERK2 time scheme at CFL = 16 and 9289 time iterations. Left column: time-longitude Hovmöller diagrams of the numerical solutions by intersecting the zonal velocity at $\theta = 44$ deg. Middle column: latitude-time Hovmöller diagrams by intersecting the zonal velocity at $\lambda = -18$ deg. Right column: dissipation analysis showing the maximum and minimum values of the total h over the full simulation. There is no visible dissipation after 100 periods. The Cubed-Sphere is $6 \times 64 \times 64$.

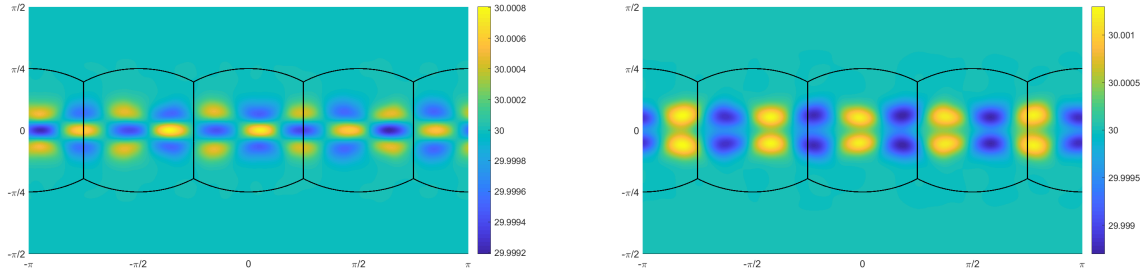


FIGURE 5. HCCS solver in space and the ERK2 time scheme. Left panel: Test 2-a (baroclinic EIG wave). The total height h is shown at final time $t = 190$ days (100 periods) with CFL = 5 and 431 time iterations. Right panel: Test 2-b (baroclinic Rossby wave). The total height is shown at final time $t = 1850$ days (100 periods) with CFL = 5 and 4313 time iterations. The solution is more concentrated near the equator than in the barotropic case. The Cubed-Sphere grid is $6 \times 64 \times 64$.

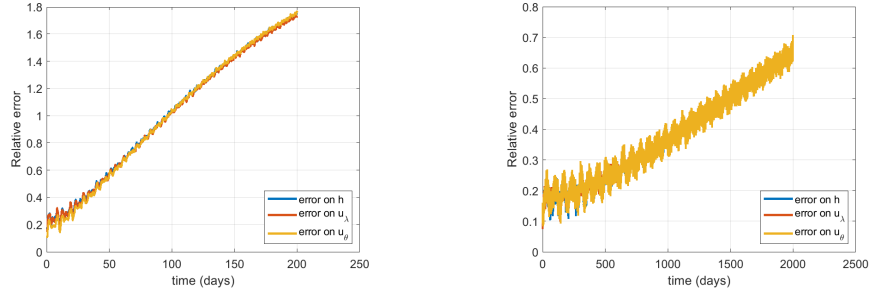


FIGURE 6. Left panel: Test 2-a (baroclinic EIG wave). Right panel: Test 2-b (baroclinic Rossby wave). The HCCS solver in space and the ERK2 time scheme are used in both cases. In both cases, the history of the relative errors for the total height h , the zonal velocity u_λ and the meridional velocity u_θ is shown. For the EIG wave, (left panel), the final time is $t = 190$ days (100 periods) with $CFL = 5$ and 431 time iterations. For the Rossby wave, (right panel), the final time is $t = 1850$ days (9100 periods) with $CFL = 5$ and 4313 time iterations. The Cubed-Sphere grid is $6 \times 64 \times 64$.

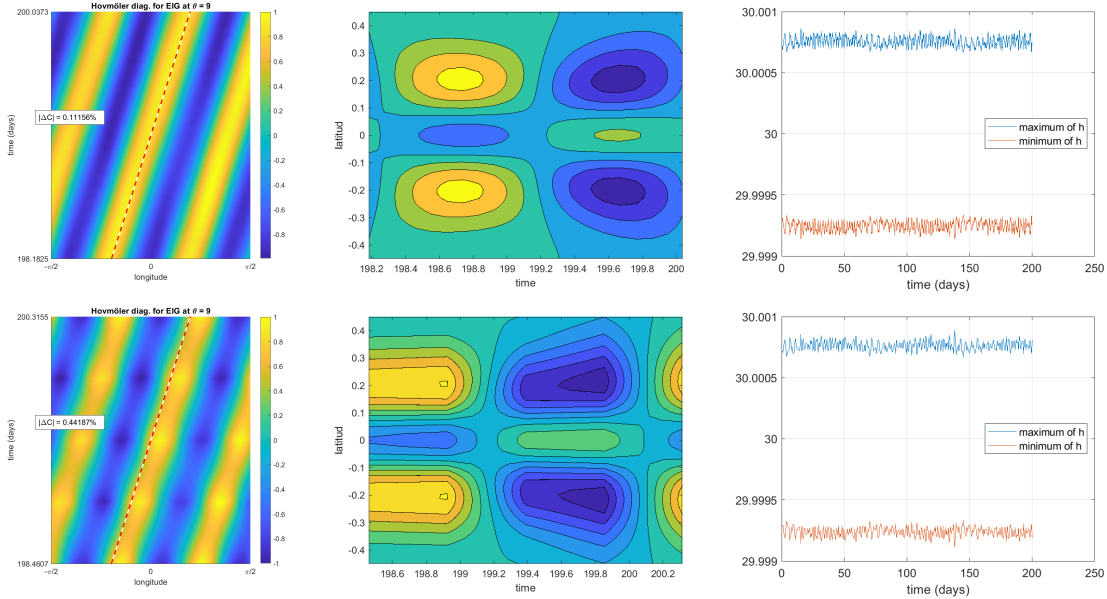


FIGURE 7. Test 2-a (baroclinic EIG wave). The HCCS solver in space is used. First line : RK4 time scheme with $CFL = 1$. Second line, ERK2 time scheme with $CFL = 5$. The first column represents time-longitude Hovmöller diagrams of the simulated solutions obtained by intersecting the zonal velocity at latitude $\theta = 9$ deg. The second column is a latitude-time Hovmöller diagram obtained by intersecting the zonal velocity at $\lambda = -18$ deg. The third column displays the maximum and minimum values of the total height h over the full simulation (final time: 190 days). The distortion in the middle panel, bottom line, is attributed to the Courant number $CFL = 5$. The Cubed-Sphere is $6 \times 64 \times 64$.

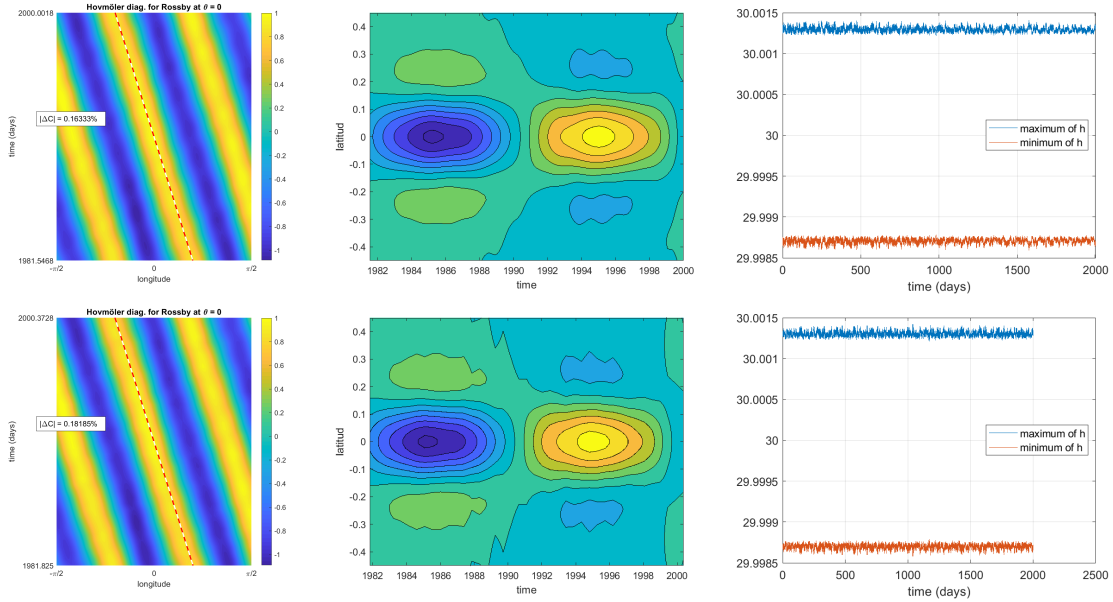


FIGURE 8. Test 2-b (baroclinic Rossby wave). First line : RK4 time scheme with Courant number CFL = 1. Second line, ERK2 time scheme with CFL = 5. The first column displays a time-longitude Hovmöller diagrams of the simulated solutions obtained by intersecting the zonal velocity at $\theta = 0$ deg. The second column displays a latitude-time Hovmöller diagrams obtained by intersection the zonal velocity at longitude $\lambda = -18$ deg. The third column represents the maximum and minimum values of h over 1850 days (100 periods). The Cubed-Sphere is $6 \times 64 \times 64$.

	<i>Test case 1</i>		<i>Test case 2</i>	
	<i>EIG wave</i>	<i>Rossby wave</i>	<i>EIG wave</i>	<i>Rossby wave</i>
CFL	4	16	5	5
Relative Mass Error	1.7666 (-14)	2.4476 (-8)	2.8297 (-15)	1.6564 (-12)
Relative Energy Error	2.6838 (-14)	4.8947 (-8)	2.2746 (-16)	3.2573 (-12)
Relative Enstrophy Error	2.5541 (-14)	3.0250 (-8)	2.0419 (-14)	2.9696 (-13)
Mean value divergence	1.5840 (-17)	3.6990 (-16)	3.6539 (-20)	6.8451 (-20)
Mean value vorticity	2.9723 (-19)	5.7501 (-25)	9.3416 (-21)	8.3526 (-21)

TABLE 3. Test 1-a, Test 1-b, Test 2-a and Test 2-b: conservation of the values in (31): mass (relative), energy (relative), enstrophy (relative), mean divergence and mean vorticity with the HCCS solver in space with the ERK2 scheme. Test 1-a (barotropic EIG wave): CFL = 4, $t = 13.5$ days, (100 periods), 407 time iterations. Test 1-b (barotropic Rossby wave): CFL = 16, $t = 1203$ days, (100 periods), 9289 time iterations. Test 2-a (baroclinic EIG wave): CFL = 5, $t = 190$ days, (100 periods), 431 time iterations. Test 2-b (baroclinic Rossby wave): CFL = 5, $t = 1850$ days, (100 periods), 4313 time iterations. In all cases, the conservation properties are very good, ranging from computer accuracy to values less than 5.10^{-8} .

- 347 Brachet, M. (2018), Schémas compacts hermitiens sur la sphère: applications en climatologie et océanographie
 348 numérique (in french), PhD thesis, Univ. Lorraine.
- 349 Brachet, M. & Croisille, J.-P. (n.d.), A center compact scheme for the Shallow Water equations on the sphere.
 350 2019, submitted.
- 351 Clancy, C. & Pudykiewicz, J. A. (2013), ‘On the use of exponential time integration methods in atmospheric
 352 models’, *Tellus A* **65**(1), 20898.
- 353 Croisille, J.-P. (2013), ‘Hermitian compact interpolation on the Cubed-Sphere grid’, *Jour. Sci. Comp.*
 354 **57**,1, 193–212.
- 355 Croisille, J.-P. (2015), ‘Hermitian approximation of the spherical divergence on the Cubed-Sphere’, *Jour.*
 356 *Comp. App. Math.* **280**, 188–201.
- 357 De-Leon, Y. & Paldor, N. (2011), ‘Zonally propagating wave solutions of Laplace tidal equations in a baroclinic
 358 ocean of an aqua-planet’, *Tellus A* **63**, 348–353.
- 359 Galewsky, J., Scott, R. & Polvani, L. (2004), ‘An initial-value problem for testing numerical models of the
 360 global shallow water equations’, *Tellus* **56**, 429–440.
- 361 Ghil, M. & Childress, S. (1987), *Topics in Geophysical Fluid Dynamics: Atmospheric dynamics, Dynamo*
 362 *theory and Climate Dynamics*, Springer.
- 363 Hairer, E. & Wanner, G. (1991), *Solving Differential equations vol. I, II*, Springer Series in Comp. Mathe-
 364 matics, Springer-Verlag.
- 365 Hovmöller, E. (1949), ‘The Trough-and-Ridge diagram’, *Tellus* **1**(2), 62–66.
- 366 Jablonowski, C. & Williamson, D. L. (2006), ‘A baroclinic instability test case for atmospheric model dy-
 367 namical cores’, *Quart. J. Roy. Meteor. Soc.* **132**, 2943–2975.
- 368 Matsuno, T. (1966), ‘Quasi-geostrophic motions in the equatorial area’, *J. Meteorol Soc. Jpn* **44**, 25–43.
- 369 Müller, D. & O’Brien, J. (1995), ‘Shallow water waves on the rotating sphere’, *Phys. Rev. E* **51**(2), 4418–4431.
- 370 Paldor, N. (2015), *Shallow Water Waves on the Rotating Earth*, Springer Brief in Earth System Sciences,
 371 Springer-Verlag.
- 372 Paldor, N., De-Leon, Y. & Shamir, O. (2013), ‘Planetary (Rossby) waves and inertia-gravity (poincaré) waves
 373 in a barotropic ocean over a sphere’, *J. Fluid Mech.* **726**, 123–136.
- 374 Portelenelle, B. & Croisille, J.-P. (2018), ‘An efficient quadrature rule on the Cubed Sphere’, *J. Comp. App.*
 375 *Math* **328**, 59–74.
- 376 Purser, R. & Rancic, M. (1998), ‘Smooth quasi-homogeneous gridding of the sphere’, *J. Comput. Phys.*
 377 **124**, 637–647.
- 378 R. D. Nair, C. J. (2008), ‘Moving vortices on the sphere: a test-case for horizontal advection problems’, *Mon.*
 379 *Wea. Rev.* **136**, 689–711.

380 Ronchi, C., Iacono, R. & Paolucci, P. S. (1996), ‘The Cubed Sphere: A new method for the solution of partial
381 differential equations in spherical geometry’, *J. Comput. Phys.* **124**, 93–114.

382 Shamir, O. & Paldor, N. (2014), ‘A Hermite-based shallow water solver for a thin ocean over a rotating
383 sphere’, *J. Comput. Phys.* **269**, 80–97.

384 Shamir, O. & Paldor, N. (2016a), ‘A Gegenbauer-based shallow water solver for a thick ocean over a rotating
385 sphere’, *J. Comput. Phys.* **304**, 487–505.

386 Shamir, O. & Paldor, N. (2016b), ‘A quantitative test case for global-scale dynamical cores based on analytic
387 wave solutions of the shallow-water equations’, *Quat. Jour. Roy. Met. Soc.* **142**, 2705–2714.

388 Shamir, O., Yacoby, I., Ziv, S. & Paldor, N. (2019), ‘The Matsuno baroclinic wave test case’, *Geo. Scient.*
389 *Dev.* **12**, 2181–2193.

390 Thuburn, J. & Li, Y. (2000), ‘Numerical simulation of Rossby-Haurwitz waves’, *Tellus* **52A**, 181–189.

391 Ullrich, P. (2011), Atmospheric Modeling with High-Order finite volume methods, PhD thesis, The Univ. of
392 Michigan.

393 Ullrich, P., Melvin, T., Jablonowski, C. & Staniforth, A. (2013), ‘A proposed baroclinic wave test case for
394 deep- and shallow-atmosphere dynamical cores’, *Quart. J. Roy. Meteor. Soc.* **140**, 1590–1602.

395 Williamson, D., Drake, J., Hack, J., Jakob, R. & Swarztrauber, P. N. (1992), ‘A standard test set for numerical
396 approximations to the shallow water equations in spherical geometry’, *J. Comput. Phys.* **102**, 211–224.

397 Williamson, D. L. (2007), ‘The evolution of dynamical cores for global atmospheric models’, *J. Meteo. Soc.*
398 *Japan* **85B**, 241–269.

399 Yee, H. & Sjögren, B. (2004), Designing adaptive low-dissipative high-order schemes for long-time inte-
400 grations, Vol. 66 of *Turbulent Flow Computation, Fluid Mechanics and its Applications*, Kluwer Acad.
401 Pub.